Thermally-stable nanocrystalline steel

C. N. Hulme-Smith*[1], S. W. Ooi[1], and H. K. D. H. Bhadeshia[1]

[1]University of Cambridge Department of Materials Science and Metallurgy, 27 Charles Babbage Road, Cambridge, CB3 0FS, U. K.

June 2, 2017

Abstract

Two novel nanocrystalline steels were designed to withstand elevated temperatures without catastrophic microstructural changes. In the most successful alloy, a large quantity of nickel was added to stabilize austenite and allow a reduction in the carbon content. A 50 kg cast of the novel alloy was produced and used to verify the formation of nanocrystalline bainite. Synchrotron X-ray diffractometry using *in-situ* heating showed that austenite was able to survive more than one hour at 773 K (500 °C) and subsequent cooling to ambient temperature. This is the first reported nanocrystalline steel with high-temperature capability.

Keywords: bainitic steel; nanocrystalline alloys; thermal stability; thermodynamic modeling; synchrotron diffraction.

---

*cns28@cam.ac.uk

1 Introduction

Nanocrystalline steels, commonly referred to as *superbainite*, have been the subject of a large number of studies since their development by Caballero et al. [1] due to their combination of strength and toughness, achieved in large volumes with neither rapid cooling nor severe deformation [1–9]. The structure consists mostly of alternating thin plates of bainitic ferrite, α_b, and retained austenite, γ_r, with a small fraction of retained austenite blocks forming the residue of the sample. The austenite films and bainite plates are typically below 50 nm in width, providing a potent strengthening mechanism without compromising toughness. The retained austenite is able to accommodate a large amount of plastic work by either one of or both dislocation glide and the formation of stress-induced martensite.

Nanocrystalline steels represent a formidable combination of mechanical properties; their transformation ultimately relies on the addition of a large quantity of carbon. Carbon serves to depress both the martensite-start temperature, M_s, and the bainite-start temperature, B_s, but the former more than the latter [2]. There is then a sufficiently wide temperature range in bainite may form with ever finer platelets as the transformation temperature is lowered.

The large carbon content is further enhanced in the retained austenite due to partitioning after the bainitic transformation. At temperatures where the atomic mobility of carbon atoms is sufficient, there will then be a tendency for the austenite to decompose into a mixture of ferrite and cementite Many studies have observed a carbon supersaturation with respect to cementite in both austenite [5, 6, 10–15] and the same applies to the ferrite containing excess carbon [12, 13, 15–19]. There is therefore a large driving force for the formation of cementite in both phases. Rapid decomposition of austenite into carbides and ferrite has been observed in nanocrystalline steels upon heating [20, 21]. The resulting loss of austenite compromises both the strength and toughness of the steel and hence it is unsuitable for service at elevated temperatures.

The aim of the current work was to design new nanocrystalline steel alloys that are able to tolerate exposure to high temperatures while retaining an acceptable level of strength and toughness.

2 Alloy Design

Two approaches were considered to develop novel alloys: an extension of previous work [22] to introduce as many atoms that are insoluble in cementite as possible and a new concept to minimize the carbon content while still obtaining the desired microstructure.

Thermodynamic modelling was conducted using the calculation software MTDATA version 4.73 from the National Physical Laboratory, Teddington, U. K. [23] with various thermodynamic databases [28, 29]. Due to the large solute concentrations envisaged, B_s temperatures were calculated using the program MTTTData [1] [23,24,29]. M_s temperatures were calculated using an artificial neural network via the software Neuromat Model Manager [25] and using a publicly-available database [2] [26]. Where a composition lay within its specified limits, M_s was calculated also using the program MUCG83 [3] [27].

2.1 Alloy 1

In a previous study it was found that a large concentration of silicon, which is insoluble in cementite, was effective in delaying the thermal decomposition of retained austenite in a nanocrystalline steel to exceptionally high temperatures during continuous heating [22]. The alloy included manganese to suppress M_s and B_s and for hardenability (Fe–1.037 C–1.97 Mn-3.89 Si–1.43 Al (wt%)). Manganese is effective in both rôles as it reduces the driving force for the transformation of austenite to ferrite, $\Delta G^{\gamma\rightarrow\alpha}$. However, manganese is also extensively soluble in cementite and so could conceivably favor cementite precipitation whereas nickel would not (figure 1). A new alloy, Alloy 1, was therefore developed to replace manganese with nickel while otherwise leaving the composition substantially unchanged.

Thermodynamic modelling showed that a nickel content of 3.3 wt % was appropriate to maintain similar B_s and M_s to the alloy studied previously. Other solutes were left substantially unchanged with the exception of the silicon content, which was increased to 4.0 wt%. The calculated equilibrium phase fractions for Alloy 1 (figure 2) shows a wide temperature range that allows the alloy to be austenitized, which is necessary to develop a homogeneous bainitic structure. The designed composition of Alloy 1 (table 1) is within the limits of the program MUCG, which predicted an M_s of 515 K (242 °C). The prediction of the artificial neural network was 423 ± 30 K (150 ± 30 °C). There is no clear reason for this discrepancy and M_s was determined to be 516 K (243 °C) using dilatometry and the offset method. The program MTTTData calculated B_s to be 623 K (350 °C).

---

[1] `http://www.msm.cam.ac.uk/map/steel/programs/MTTTDATA.html`

[2] `http://www.msm.cam.ac.uk/map/data/materials/Ms_data_2004.html`

[3] `http://www.msm.cam.ac.uk/map/steel/programs/mucg83.html`

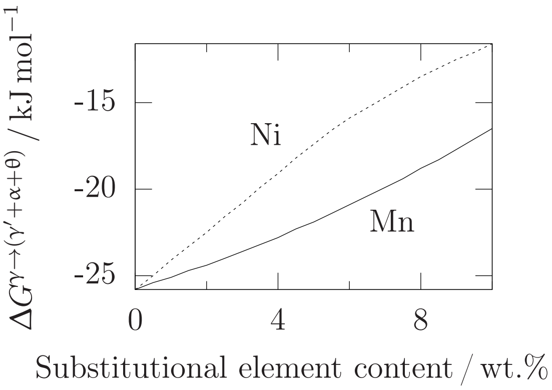

Figure 1: Driving force for the decomposition of austenite, γ, to a paraequilibrium mixture of carbon-depleted austenite, γ', ferrite, α and cementite, θ, calculated in Fe–1.0 wt% C–x at 773.15 K (500.00 °C) [23, 28].

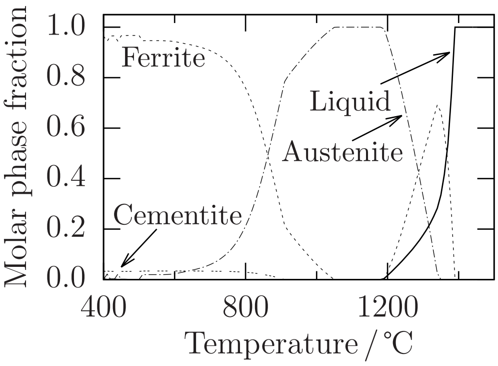

Figure 2: Calculated equilibrium phase fractions for Alloy 1 allowing liquid, austenite, ferrite and cementite only [23, 29]. No other phases were anticipated to form.

	C	Mn	Al	Ni	Si	Co	Mo
Alloy 1	0.7	0.02	1.4	3.3	4.0	—	0.25
Alloy 2	0.4	0.15	2.5	13.0	—	4.0	0.3

Table 1: Designed compositions of new alloys. All values are in wt%.

2.2 Alloy 2

Although previous work [22] has shown that the addition of large amount of cementite-insoluble elements can delay the thermal decomposition, it is unlikely that such an approach can sufficiently suppress cementite precipitation: ultimately, a mixture of ferrite and cementite is required by equilibrium. A novel approach was therefore considered: to minimize the carbon content of retained austenite and thereby reduce the driving force for the precipitation of carbides. Significant quantities of substitutional austenite stabilizer (other than manganese) must then be added to both prevent ferrite formation at high temperatures and to reduce the amount of carbon enrichment in austenite during the bainite transformation. Nickel, which is a powerful substitutional austenite stabilizer that can be exploited for this purpose [30].

Thermodynamic calculations showed that the composition listed in table 1 can be fully austenitized and has a calculated B_s of 643 K (370 °C) and M_s of 363 K (90 °C) [23, 24, 29]. The neural network model predicts an M_s of 413 K (160 °C) [25, 26]. These values are consistent with previously-reported nanocrystalline bainitic steels [1–6]. The carbon content of 0.4 wt% was chosen to provide a suitable interval between B_s and M_s such that a large volume fraction of bainite may be formed [30]. Besides iron, carbon and nickel, Alloy 2 includes aluminium to both accelerate the bainite transformation and provide some resistance to cementite precipitation, cobalt to further accelerate the bainite transformation and of manganese and molybdenum to tie up sulphur and phosphorus impurities, respectively, but in quantities small enough not to have other metallurgical consequences [23, 28]. The level of aluminium is limited so that the B_s and M_s remain suppressed to temperatures where nanostructured bainite can be obtained (table 1).

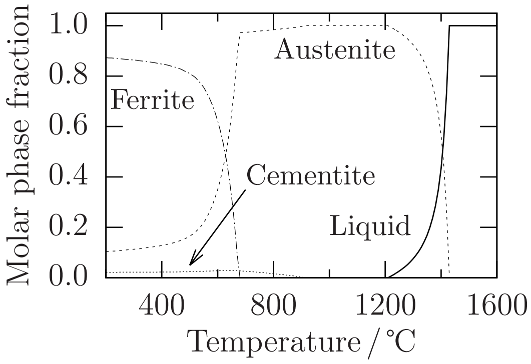

Figure 3: Calculated equilibrium phase fractions for Alloy 2 allowing liquid, austenite, ferrite and cementite only [23, 29]. No other phases were anticipated to form.

A lower bound for the amount of carbon in solution in retained austenite is derived using the thermodynamic quantity $x_{T'_0}$, the carbon content at which austenite and ferrite have the same free energy at a given temperature once the strain energy of transformation has been accounted for. Should the carbon content of austenite reach this value, further diffusionless transformation to ferrite is thermodynamically impossible. The expected x_{T_0} of Alloy 2 is significantly lower at a given temperature than that of Alloy 1 (figure 4).

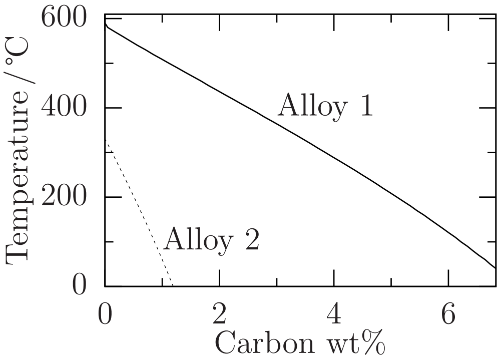

Figure 4: The temperature-dependent values of $x_{T'_0}$ for both Alloy 1 and Alloy 2 calculated MTTTData [23, 24, 29]. Data are calculated only for $273\,\text{K} < T < B_\text{s}$ ($0\,°\text{C} < T < B_\text{s}$). Alloy 2 is expected to form retained austenite with a lower carbon content than Alloy 1 at a given transformation temperature.

Apart from limiting the amount of carbon enrichment in austenite, a high nickel content stabilizes the retained austenite with respect to ferrite. This is especially important during exposure to elevated temperature when carbides are able to precipitate. The resulting depletion of carbon in the retained austenite has been shown to lead to the formation of more ferrite, both during isothermal holding and during subsequent cooling [20,21]. It is expected that the high nickel content of Alloy 2 will prevent this transformation and allow the alloy to avoid carbide precipitation during thermal exposure.

3 Experimental Methods

3.1 As-transformed microstructures

Samples of both alloys, measuring 10 mm × 10 mm × 80 mm and of the measured composition given in table 2 were heated in a vacuum tube furnace to 1273 K (1000 °C) to form austenite. After 30 min, the samples were removed and agitated in air until no glowing was observed, at which point, they were assumed to be no hotter than 798 K (525 °C) [31]. They were then transferred to a high-precision oven at 523 K (250 °C) for 14 d (Alloy 2) or 1 d (Alloy 1). The resulting microstructures (figure 5) show that a homogeneous microstructure of nanocrystalline bainite has formed.

Representative SEM images were analyzed using the software ImageJ to derive the grain widths of the austenite and ferrite films using the mean lineal intercept method [32]. Twenty measurements were made for each phase in each sample. The grains were assumed to be plate-shaped and the measured intercept was multiplied by a stereological correction factor of $\frac{\pi}{2}$ [33, 34].

3.2 Thermal Stability

The thermal stability of both alloys was assessed by synchrotron X-ray diffractometry with *in-situ* heating. Experiments were performed at beamline I12 at Diamond Light Source, Didcot, U. K. 3 mm diameter rods were sealed into glass ampoules filled with argon, austenitized at 1273 K (1000 °C) for 30 min and transformed to bainite at 523 K (250 °C). The samples of Alloy 1 were allowed to transform for 24 h and those of Alloy 2 for 14 d. Tempering was performed using a bespoke halogen lamp furnace with X-ray transparent windows. The temperature was controlled using a thermocouple on the surface of the sample and close to the X-ray beam. The windows for the diffracted beam had a radius of 10 mm and were approximately 100 mm from the center of the sample. X-rays that did not pass through the windows were heavily attenuated. 2θ was thus limited to approximately 5.7°. A photon energy of 120 keV (equivalent to a wavelength of 0.103 Å) was chosen to ensure enough peaks were detected to allow Rietveld refinement to be performed.

X-ray detection was attained by a Thales Pixium RF4343 large-area 2D detector with pixels 148 µm × 148 µm positioned perpendicular to the X-ray beam and 1500 mm from the sample. The line broadening behavior of the beamline was calibrated using a ceria standard. Calibrations were performed at both the beginning and end of the experiment after Hart et al. [35].

The X-ray beam size was optimized to 0.5 mm × 0.5 mm, which gives sufficient angular resolution to resolve all peaks while maintaining the maximum practicable detected intensity, so allowing data to be recorded as often as possible. Data were collected every 4 s.

Samples were heated from ambient temperature to 773 K (500 °C) at $10\,\mathrm{K\,min^{-1}}$ ($10\,^{\circ}\mathrm{C\,min^{-1}}$). The temperature was maintained until it was deemed that no further change in diffraction rings was likely. The samples were then allowed to cool in air to ambient temperature at $20\,\mathrm{K\,min^{-1}}$ ($20\,^{\circ}\mathrm{C\,min^{-1}}$).

Data were acquired as 24-bit TIFF images, which were integrated using graphical analysis software Fit2D [36]. Integrated data were then subjected to Rietveld refinement analysis using the software Materials Analysis Using Diffraction (MAUD) [38–40]. For the purposes of Rietveld analysis, the material was assumed to consist of austenite and ferrite only. A fifth-order polynomial background function, incident X-ray intensity, the lattice parameters, crystallite size and microstrain of both phases and the volume fraction of austenite were allowed to refine. The volume fraction of ferrite was set to be the residue of the sample.

4 Results

4.1 Measured composition

Chemical analysis during production resulted in the measured compositions in table 2.

	C	Mn	Al	Ni	Si	Co	Mo
Alloy 1	0.72	0.02	1.38	3.40	3.88	—	0.20
Alloy 2	0.45	0.15	2.63	13.2	0.03	3.99	0.30

Table 2: Compositions of novel alloys, as measured during cast production. All values are wt%.

4.2 As-transformed microstructures

It may be seen that both alloys produce homogeneous, nanocrystalline bainitic structures (figure 5). Analysis of the width of retained austenite films and bainitic ferrite platelets showed that both phases were finer in Alloy 1 than Alloy 2 (table 3), but that the difference was well within the uncertainty of the measurement.

	Grain size / nm	
	γ_r	α_b
Alloy 1	70 ± 30	80 ± 50
Alloy 2	100 ± 30	140 ± 50

Table 3: Stereologically-corrected grain widths, measured perpendicular to the long axis of each plate for samples transformed at 523 K (250 °C). Errors are the standard deviation of the individual measurements.

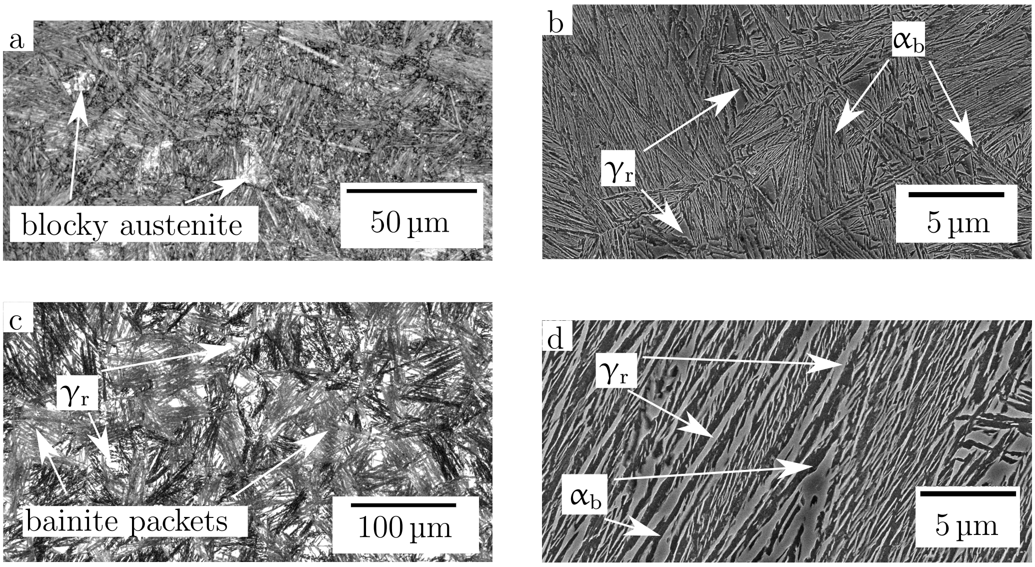

Figure 5: Structures after transformation of a, b Alloy 1 and c, d Alloy 2. The high-magnification images demonstrate that the transformation product is nanocrystalline bainite in both cases and the low-magnification micrographs show that the structures of both alloys are homogeneous.

4.3 Thermal Stability

Inspection of the integrated data shows that while all peaks initially shift to lower Bragg angles due to thermal expansion during heating, the austenite peaks in Alloy 1 shift suddenly to slightly higher Bragg angles after approximately 3 ks (equivalent to the sample reaching 773 K (500 °C)) and thereupon rapidly disappear (figure 6a). The ferrite peaks simultaneously become more intense and additional peaks corresponding to carbides appear. All carbide and ferrite peaks shift to higher Bragg angles during cooling. In Alloy 2, all peaks initially shift to lower Bragg angles, but the austenite peaks do not then disappear (figure 6b). Both austenite and ferrite peaks shift to higher Bragg angles during cooling. Austenite peaks are still present at the conclusion of the experiment, at which time the sample is at ambient temperature.

Closer inspection of the Rietveld refinement results for austenite shows a large contraction in austenite lattice parameter of Alloy 1, which is immediately followed by the reduction of the austenite volume fraction until austenite is almost lost form the material (figure 7a). In Alloy 2, the austenite lattice parameter drops slightly at 2.8 ks to a new steady value. Similarly, the volume fraction decreases to a new steady value (figure 7b). It is clear

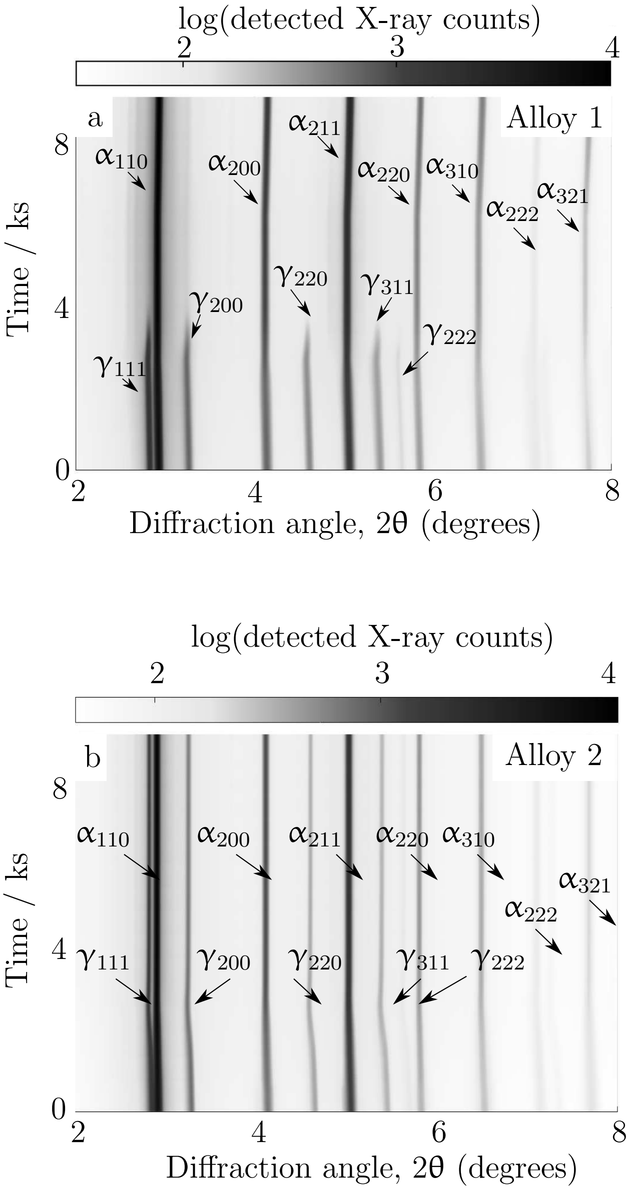

Figure 6: Integrated XRD data for tempering experiments at Diamond Light Source. (a) the peaks attributed to austenite disappear upon heating in Alloy 1, but (b) persist throughout the experiment in Alloy 2.

that austenite in Alloy 2 has survived the heat treatment. In both alloys, peaks that formed during tempering could be attributed to cementite, consistent with previous observations in literature [41].

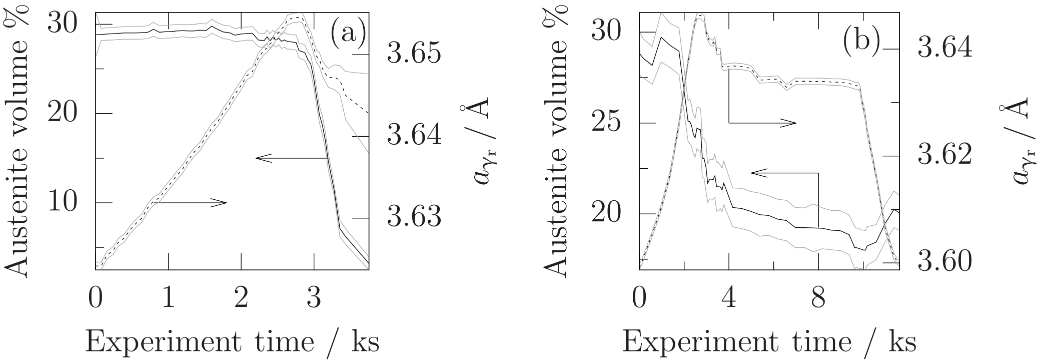

Figure 7: Austenite volume fractions and lattice parameters derived using Rietveld refinement from the synchrotron XRD data for (a) Alloy 1 and (b) Alloy 2. The austenite in Alloy 1 undergoes thermal expansion before contracting sharply whereupon it is lost. In Alloy 2 the austenite contracts slightly and partially transforms. The remaining austenite then persists for the remainder of the experiment.

	V_{γ_r} (%)	
	As-transformed	Thermally-exposed
Alloy 1	29 ± 3	3.0 ± 0.7
Alloy 2	28.8 ± 1.2	20.0 ± 1.0

Table 4: Retained austenite volume fraction, V_{γ_r} for both alloys measured before and after thermal exposure during synchrotron experiments.

Examination of the microstructures of the alloys after the *in-situ* experiments confirm the XRD findings that austenite is lost in Alloy 1 but persists, albeit at a lower volume fraction, in Alloy 2. The as-transformed microstructure of Alloy 1 has been completely destroyed (figure 8a) but are still present in Alloy 2 (figure 8b). A close examination of austenite films in a sample of Alloy 2 transformed to bainite at 498 K (225 °C) and exposed to the same tempering treatment reveals that some of them contain martensite plates, α' (figure 8c). Such features were not observed during extensive examination of as-transformed Alloy 2.

		a_{γ_r} / nm	
	As-transformed	Peak	Thermally-exposed
Alloy 1	3.6251 ± 0.0005	3.6546 ± 0.0006	3.6127 ± 0.0012
Alloy 2	3.5992 ± 0.0005	3.6463 ± 0.0007	3.5998 ± 0.0005

Table 5: Retained austenite lattice parameter, a_{γ_r}, for both alloys measured before and after thermal exposure during synchrotron experiments. The peak lattice parameter, measured at 500 ℃, is also reported.

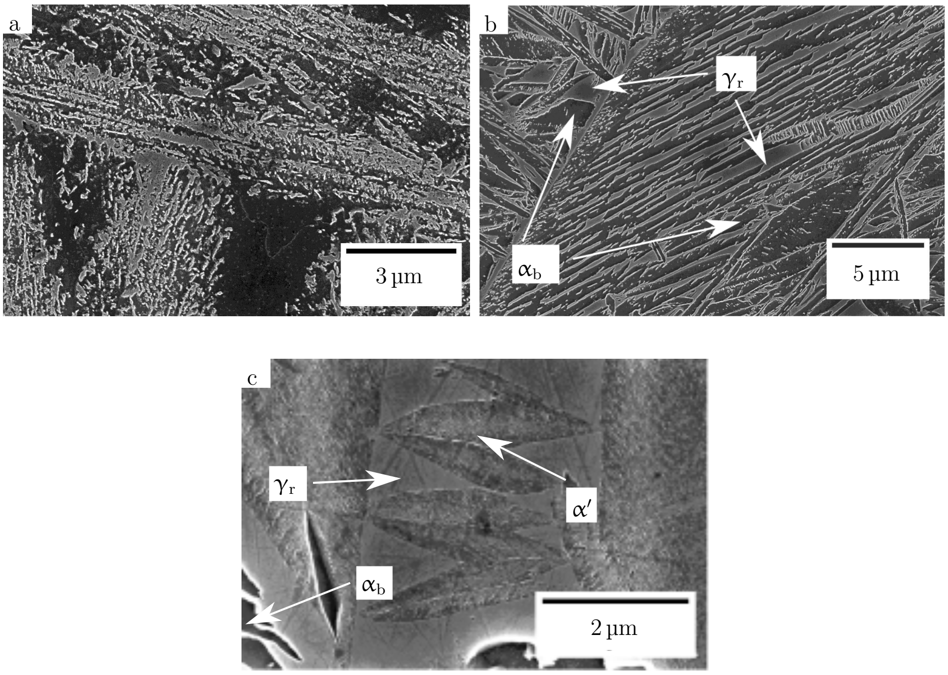

Figure 8: Scanning electron micrographs of (a) Alloy 1; (b) and (c) Alloy 2. The microstructure of Alloy 1 is radically changed from the as-transformed condition with bright carbides forming in place of retained austenite. Alloy 2 is largely unchanged, save for the formation of martensite in some retained austenite films.

5 Discussion

The as-transformed structures are nanocrystalline bainite, consistent with the calculated transformation properties. The larger crystal size of Alloy 2 (table 3) is also in line with bainite transformation theory as its lower carbon content renders the parent austenite weaker than that of Alloy 1. This allows more plastic deformation to occur and bainitic ferrite plates are able to grow larger before being stifled by work hardening. The composition of Alloy 2 also aids this effect, since both nickel and aluminium lower the cross-slip energy in austenite while silicon increases it [42, 43]. Increasing the stacking fault energy causes dislocations to cross-slip more easily and reduces the rate of work hardening. Although the grain sizes in Alloy 2 appear to be larger than those typically associated with nanocrystalline bainitic steel, the transformation has taken place at a temperature consistent with such alloys in literature and the structure is certainly bainitic. Furthermore, the difference between grain size of Alloy 2 and those typical of steels in previously-published work is within the error of the current measurements. The authors therefore consider Alloy 2 to be a nanocrystalline bainitic steel.

The apparent thermal stability of Alloy 2 validates the design process. Analysis of the carbide peaks identifies cementite as the main carbide, accounting for almost all additional peaks, consistent with the absence of silicon.

Tensile test results indicate that the 0.2% proof stress of Alloy 1 increases from 1490 ± 50 MPa to 1767 MPa as a result of tempering at 450 °C for 8 d (two samples of each condition were tested, but proof stress could only be assessed in one of the the tempered samples, so no experimental uncertainty may be assessed). In Alloy 2, the same heat treatment caused a rise in 0.2% proof stress from 1011 ± 5 MPa to 1603 ± 12 MPa. Although tempering is usually expected to soften material, the current data are consistent with previously-reported tempering experiments in nanocrystalline bainitic steels due to tempering, where ductile austenite decomposes into less-ductile ferrite and carbides without significant grain coarsening [44]. The larger grain size of Alloy 2 contributes significantly to its lower tensile strength relative to Alloy 1: the fine grain size leads to strengthening via the mechanism of Langford and Cohen [45]. Increasing the grain size in the austenite from 70 nm to 100 nm leads to a reduction in strength of approximately 500 MPa. Since austenite is the more ductile phase, its strength will limit that of the alloy. Mechanical properties of the current alloys will be discussed in detail in future work.

The apparent stability of Alloy 2 may be explained by its high nickel content. It has been observed that the first step in austenite decomposition is the loss of carbon, either to carbides [21] or to defects [47]. While carbon is able to diffuse a significant distance in the tempering process (4 µm in austenite with a high-nickel environment [46]), substitutional alloying elements are not. For example, both nickel and cobalt may diffuse approximately 1 Å in 1 h at 500 °C and iron 2 Å [48]. This means that while the amount of carbon in solid solution may decrease during the tempering experiments, the amount of substitutional solute may not. Examination of the austenite lattice parameters (table 5) reveals that the loss of carbon from solid solution is much more pronounced in Alloy 1 than Alloy 2: the former undergoes a contraction consistent with the loss of carbon from solid solution whereas the latter does not change significantly. This implies that the dissolved carbon content in the former decreases greatly, while that in the latter undergoes no significant change [49]. The smaller starting lattice parameter of Alloy 2 further indicates that the amount of carbon in solid solution is lower than in Alloy 1. Since the large nickel content of Alloy 2 reduces the driving force for the transformation of austenite to ferrite (figure 1), the driving force is not sufficient to grow ferrite from the tempered austenite and so the austenite persists throughout tempering and subsequent cooling to room temperature, despite the precipitation of carbides (table 4).

6 Conclusions

Two novel nanocrystalline bainitic steels have been designed and produced. Austenitization at 1273 K (1000 °C) and transformation at 523 K (250 °C) resulted in a homogeneous, bainitic microstructure consisting of an intimate mixture of bainitic ferrite films, retained austenite films and retained austenite blocks. Time-resolved *in-situ* synchrotron X-ray diffractometry during tempering of the as-transformed material showed that the austenite persists in Alloy 2 during tempering at 773 K (500 °C) for 1 h and throughout subsequent cooling to room temperature. This is the first nanocrystalline bainitic steel in which austenite is not completely lost during tempering and cooling. Such a material, with the combination of strength and toughness typical of similar alloys along with thermal stability has potential for use in high-temperature engineering applications.

Acknowledgements

The authors would like to thank Diamond Light Source for beamtime (proposal EE9880) and the staff of beamline I12 for assistance with the acquisition of the time-resolved data presented in this paper. The authors would also like to thank Rolls-Royce plc and the Engineering and Physical Sciences Research Council for providing funding for the current work (grant number RG64823).

References

[1] F. G. Caballero, H. K. D. H. Bhadeshia, K. J. A. Mawella, D. G. Jones, P. M. Brown: *Mater. Sci. Technol.*, 2002, vol. 18, pp. 279-284.

[2] H. K. D. H. Bhadeshia: *Solid→Solid Phase Transform. Inorg. Mater., Proc. Int. Conf.*, 2005, pp. 469-484.

[3] C. García-Mateo, F. G. Caballero, H. K. D. H. Bhadeshia: *J. Phys. IV*, 2003, vol. 112, pp. 285–288.

[4] C. García-Mateo, F. G. Caballero, H. K. D. H. Bhadeshia: *ISIJ Int.*, 2003, vol. 43, pp. 1821–1825.

[5] C. García-Mateo, M. J. Peet, F. G. Caballero, H. K. D. H. Bhadeshia: *Mater. Sci. Technol.*, 2004, vol. 20, pp. 814–818.

[6] M. J. Peet, S. S. Babu, M. K. Miller, H. K. D. H. Bhadeshia: *Scripta Mater.*, 2004, vol. 50, pp. 1277–1281.

[7] M. N. Yoozbashi, S. Yazdani: *Mater. Sci. Eng. A*, 2010, vol. 527, pp. 3200–3205.

[8] E. Skołek, S. Marciniak, W. A. Świątnicki: *Arch. Metall. Mater.*, 2015, vol. 60, pp. 1–6.

[9] H. Hu, H. S. Zurob, G. Xu, D. Embury, G. R. Purdy: *Mater. Sci. Eng. A*, 2015, vol. 626, pp. 34–40.

[10] F. G. Caballero, M. K. Miller, S. S. Babu, C. García-Mateo: *Acta Mater.*, 2007, vol. 55, pp. 381–390.

[11] F. G. Caballero, M. K. Miller, C. García-Mateo, C. Capdevila, S. S. Babu: *Acta Mater.*, 2008, vol. 56, pp. 188–199.

[12] F. G. Caballero, M. K. Miller, A. J. Clarke, C. García-Mateo: *Scripta Mater.*, 2010, vol. 63, pp. 442–445.

[13] F. G. Caballero, H.-W. Yen, M. K. Miller, J.-R. Yang, J. Cornide, C. García-Mateo: *Acta Mater.*, 2011, vol. 59, pp. 6117–6123.

[14] F. G. Caballero, M. K. Miller, C. García-Mateo: *Metall. Mater. Trans. A*, 2011, vol. 42, pp. 3660–3668.

[15] F. G. Caballero, C. García-Mateo, M. K. Miller: *J. Mater.*, 2014, vol. 66, pp. 747–755.

[16] F. G. Caballero, M. K. Miller, C. García-Mateo: *Acta Mater.*, 2010, vol. 58, pp. 2338–2343.

[17] F. G. Caballero, M. K. Miller, C. García-Mateo, J. Cornide, M. J. Santofimia: *Scripta Mater.*, 2012, vol. 67, pp. 846–849.

[18] F. G. Caballero, M. K. Miller, C. García-Mateo, J. Cornide: *J. Alloys Compd.*, 2013, vol. 577, pp. S626–S630.

[19] C. N. Hulme-Smith, I. Lonardelli, A. C. Dippel, H. K. D. H. Bhadeshia: *Scripta Mater.*, 2013, vol. 69, pp. 409–412.

[20] A. Saha Podder, H. K. D. H. Bhadeshia: *Mater. Sci. Technol. A*, 2010, vol. 527, pp. 2121–2128.

[21] A. Saha Podder: PhD Thesis, University of Cambridge, U. K., 2011.

[22] C. N. Hulme-Smith, I. Lonardelli, M. J. Peet, A. C. Dippel, H. K. D. H. Bhadeshia: *Scripta Mater.*, 2013, vol. 69, pp. 191–194.

[23] R. H. Davies, A. T. Dinsdale, J. A. Robinson, S. M. Martin: *CALPHAD*, 2002, vol. 26, pp. 229–271

[24] T. Okumura, T. Sourmail: MTTTData. , (University of Cambridge 2004). `https://www.msm.cam.ac.uk/map/steel/programs/MTTTDATA.html` Accessed 25 September 2013.

[25] T. Sourmail: Neuromat Model Manager. (2004). Accessed 14 September 2013.

[26] T. Sourmail, C. García-Mateo: MAP martensite start temperature data library. (University of Cambridge 2004), `http://www.msm.cam.ac.uk/map/data/materials/Ms_data_2004.html`. Accessed 3 April 2016.

[27] M. J. Peet, H. K. D. H. Bhadeshia: mucg83. (University of Cambridge, 2006), `http://www.msm.cam.ac.uk/map/steel/programs/mucg83.html`. Accessed 14 Aug 2016.

[28] SGTE (Scientific Group Thermodynamic Europe) thermodynamic database for steels, version 4.2, 2006.

[29] PLUS thermodynamic database, version 3.02, National Physical Laboratory, Teddington, U. K., 1993

[30] H. K. D. H. Bhadeshia, R. W. K. Honeycomb: *Steels*, 3rd ed., Elsevier, Oxford, U. K., 2006, pp. 74.

[31] J. W. Draper: *Philos. Mag.*, 1847, vol. 30, pp. 345–360.

[32] C. A. Schneider, W. S. Rasband, K. W. Eliceiri: *Nat. Methods*, 2012, vol. 9, pp. 671–675.

[33] L. C. Chang, H. K. D. H. Bhadeshia: *Mater. Sco. Technol.*, 1995, vol. 11,pp. 874–882.

[34] C. Mack, M. S. Bartlett: *Math. Proc. Cambridge Philos. Soc.*, 1956, vol. 52, pp. 246–250.

[35] M. L. Hart, M. Drakopoulos, C. Reinhard, T. Connolley: *J. Appl. Crystallogr.*, 2013, vol. 46, pp. 1249–1260.

[36] A. P. Hammersley: Report no. ESRF97HA02T, ESRF, Grenoble, France, 1997.

[37] A. P. Hammersley, S. O. Svensson, M. Hanfland, A. N. Fitch, D. Häusermann: *High Pressure Res.*, 1996, vol. 14, pp. 235–248.

[38] L. Lutterotti, S. Matthies, H.-R. Wenk: *roc. Int. Conf. Textures Mater.*, 12th, 1999, pp. 1599.

[39] L. Lutterotti, S. Matthies, H.-R. Wenk: *Newsl. Comm. Powder Diffr.*, 1999, vol. 21, pp. 14–15.

[40] R. A. Young: *The Rietveld Method*, Oxford University Press, Oxford, U. .K, 1993.

[41] C. Bellot, P. Lamesle, D. Delagnes, *Acta Metall. Sin.*, vol. 26, 2013, pp. 553557.

[42] R. E. Schramm, R. P. Reed: *Metall. Trans. A*, 1975, vol. 6, pp. 1345–1351.

[43] G. R. Lehnhoff, K. O. Findley, B. C. De Cooman: *Scripta Mater.*, 2014, vol. 92, pp. 19–22.

[44] C. García-Mateo, M. J. Peet, F. G. Caballero, H. K. D. H. Bhadeshia: *Mater. Sci. Technol.*, 2004, vol. 20, pp. 814818.

[45] G. Langford, M. Cohen: *Metall. Trans.*, vol. 1, 1970, pp. 14781480.

[46] P. Thibaux, A. Métenier, C. Xhoffer: *Metall. Mater. Trans. A*, vol. 38, 2007, pp. 1169–1176.

[47] C. Y. Chen, C. C. Chen, J. S. Lin: *Int. J. Mech. Ind. Sci. Eng.*, vol. 8, 2014, pp. 876879.

[48] J. Fridberg, L.-E. Törndahl, M. Hillert: *Jernkont. Ann.*, vol. 153, 1969, pp.263–276.

[49] D. J. Dyson, B. Holmes: *J Iron Steel Inst*, vol. 208, 1970, pp. 469–474.

Figure captions

1. Driving force for the decomposition of austenite, γ, to a paraequilibrium mixture of carbon-depleted austenite, γ', ferrite, α and cementite, θ, calculated in Fe–1.0 wt% C–x at 773.15 K (500.00 °C) [23, 28].

2. Calculated equilibrium phase fractions for Alloy 1 allowing liquid, austenite, ferrite and cementite only [23,29]. No other phases were anticipated to form.

3. Calculated equilibrium phase fractions for Alloy 2 allowing liquid, austenite, ferrite and cementite only [23,29]. No other phases were anticipated to form.

4. The temperature-dependent values of $x_{T_0'}$ for both Alloy 1 and Alloy 2 calculated MTTTData [23,24,29]. Data are calculated only for $273\,\mathrm{K} < T < B_\mathrm{s}$ ($0\,^\circ\mathrm{C} < T < B_\mathrm{s}$). Alloy 2 is expected to form retained austenite with a lower carbon content than Alloy 1 at a given transformation temperature.

5. Structures after transformation of a, b Alloy 1 and c, d Alloy 2. The high-magnification images demonstrate that the transformation product is nanocrystalline bainite in both cases and the low-magnification micrographs show that the structures of both alloys are homogeneous.

6. Integrated XRD data for tempering experiments at Diamond Light Source. (a) the peaks attributed to austenite disappear upon heating in Alloy 1, but (b) persist throughout the experiment in Alloy 2.

7. Austenite volume fractions and lattice parameters derived using Rietveld refinement from the synchrotron XRD data for (a) Alloy 1 and (b) Alloy 2. The austenite in Alloy 1 undergoes thermal expansion before contracting sharply whereupon it is lost. In Alloy 2 the austenite contracts slightly and partially transforms. The remaining austenite then persists for the remainder of the experiment.

8. Scanning electron micrographs of (a) Alloy 1; (b) and (c) Alloy 2. The microstructure of Alloy 1 is radically changed from the as-transformed condition with bright carbides forming in place of retained austenite. Alloy 2 is largely unchanged, save for the formation of martensite in some retained austenite films.

Table captions

1. Designed compositions of new alloys. All values are in wt%.
2. Compositions of novel alloys, as measured during cast production. All values are wt%.
3. Stereologically-corrected grain widths, measured perpendicular to the long axis of each plate for samples transformed at 523 K (250 ℃). Errors are the standard deviation of the individual measurements.
4. Retained austenite volume fraction, V_{γ_r} for both alloys measured before and after thermal exposure during synchrotron experiments.
5. Retained austenite lattice parameter, a_{γ_r}, for both alloys measured before and after thermal exposure during synchrotron experiments. The peak lattice parameter, measured in both cases at 500 ℃, is also reported.

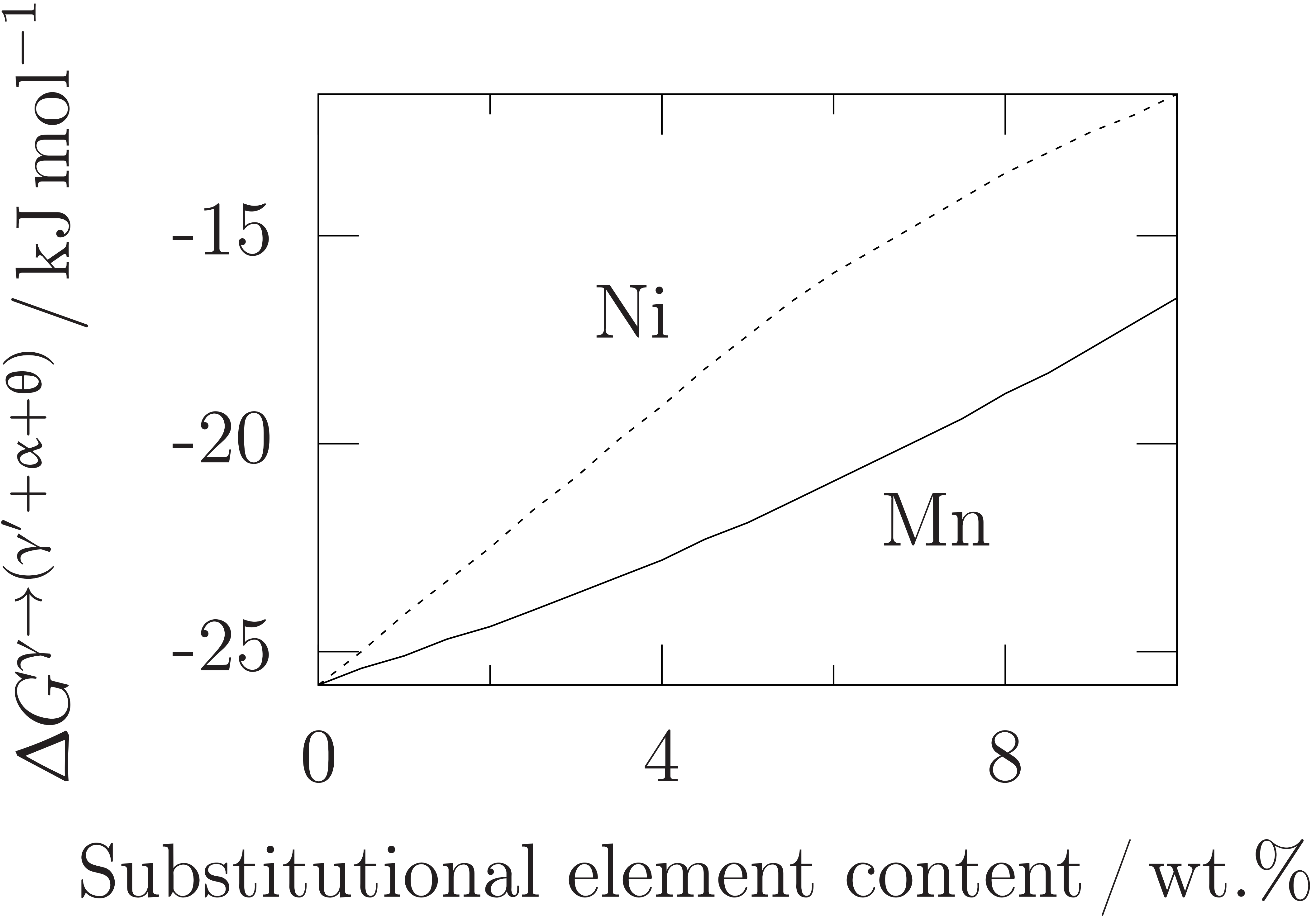
$\Delta G^{\gamma\rightarrow(\gamma'+\alpha+\theta)}$ / kJ mol^{-1}
-15
-20
-25
0
4
8
Ni
Mn
Substitutional element content / wt.%

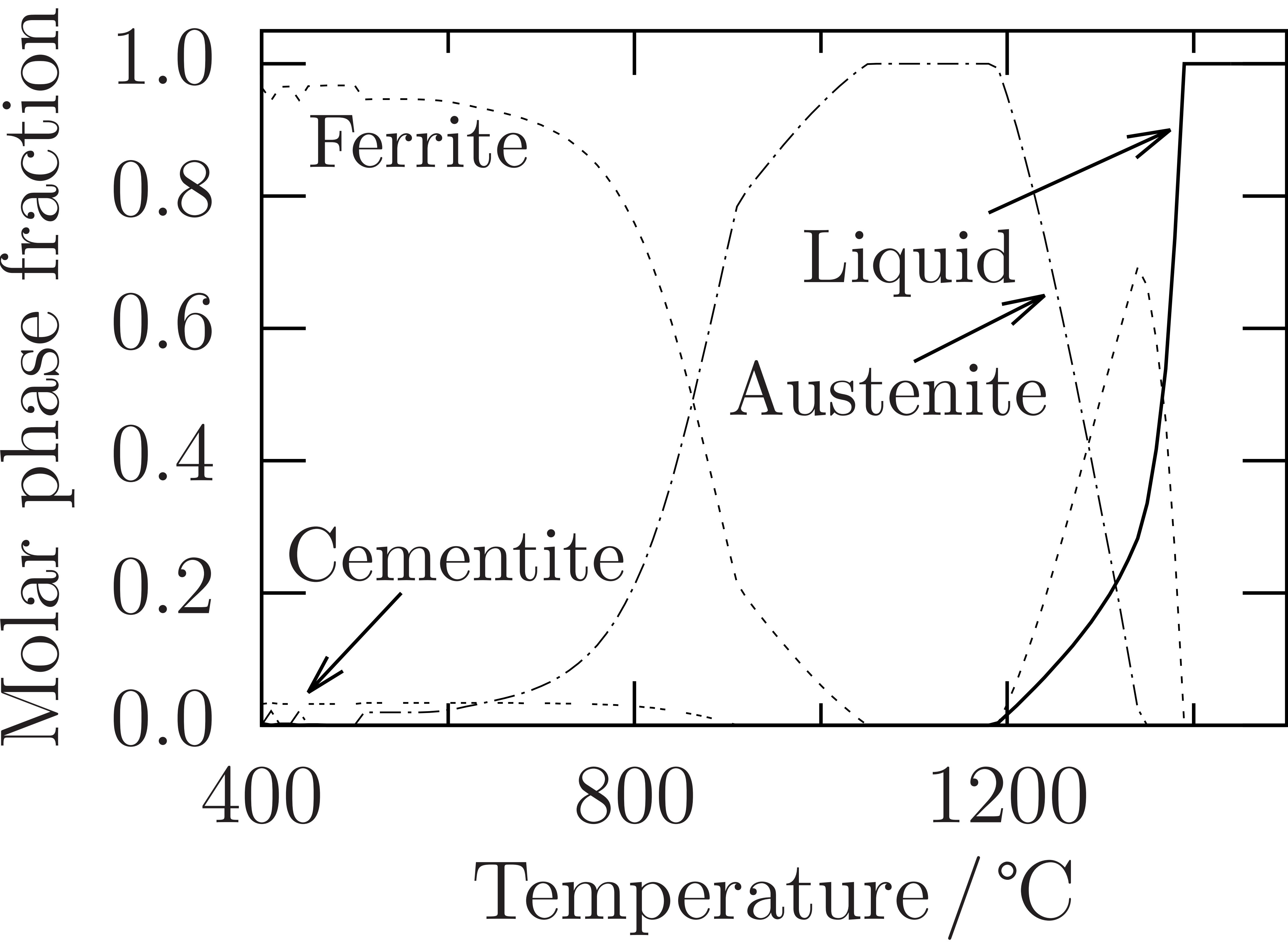
Molar phase fraction
1.0
0.8
0.6
0.4
0.2
0.0
400
800
1200
Temperature / °C
Ferrite
Cementite
Liquid
Austenite

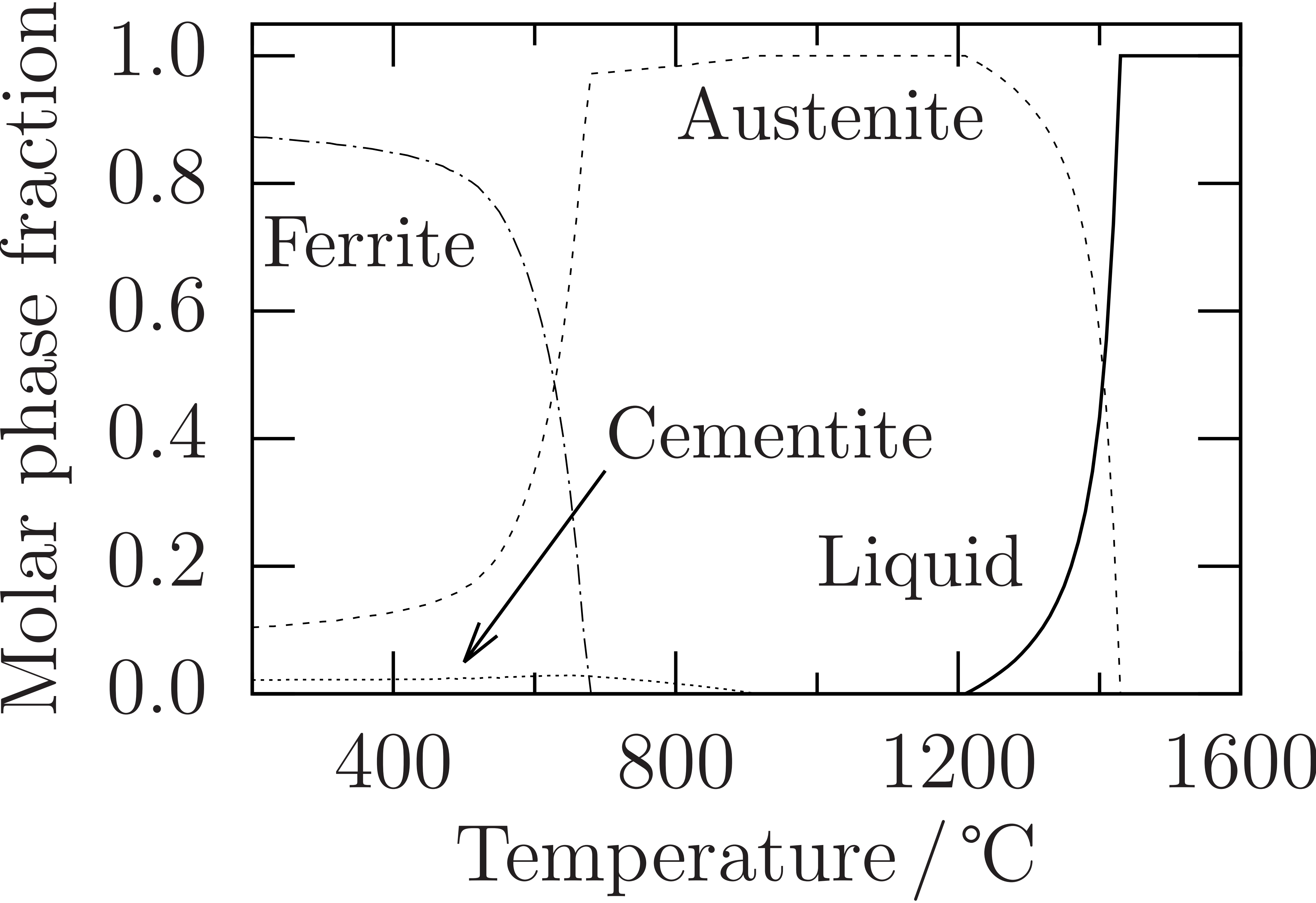
Molar phase fraction
1.0
0.8
0.6
0.4
0.2
0.0
400
800
1200
1600
Temperature / °C
Austenite
Ferrite
Cementite
Liquid

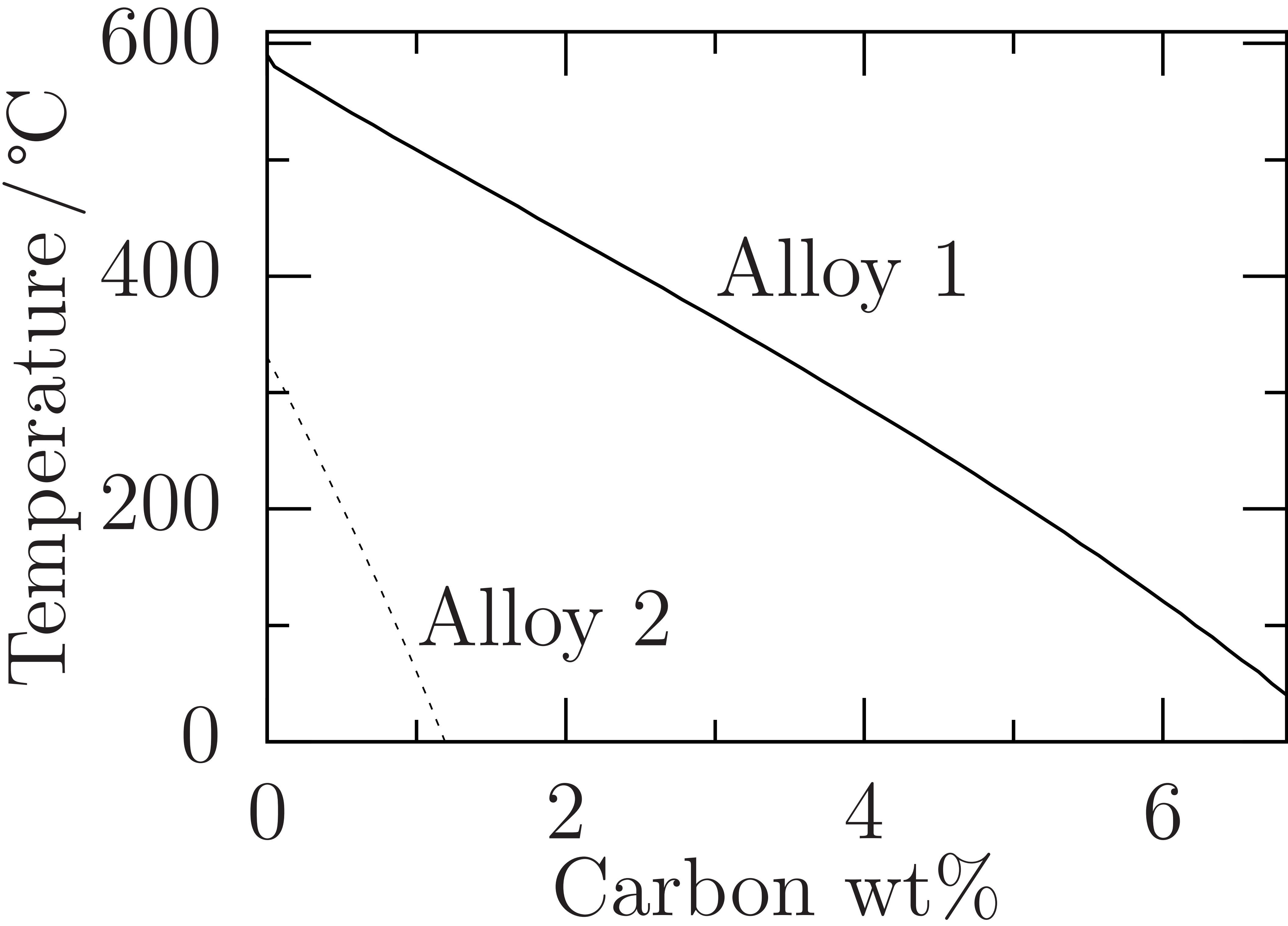
600
400
200
0
Temperature / °C
0
2
4
6
Carbon wt%
Alloy 1
Alloy 2

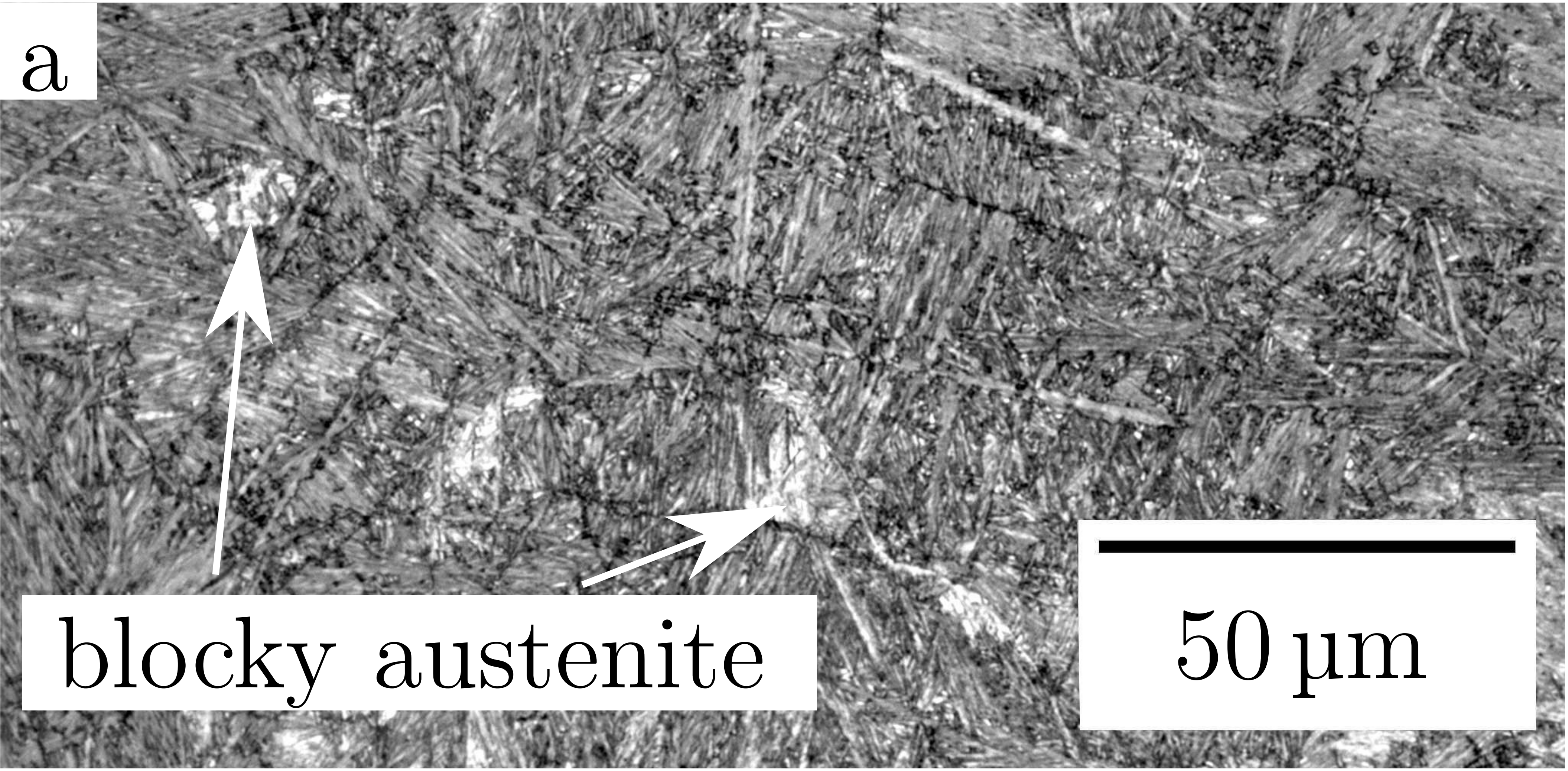
a
blocky austenite
50 µm

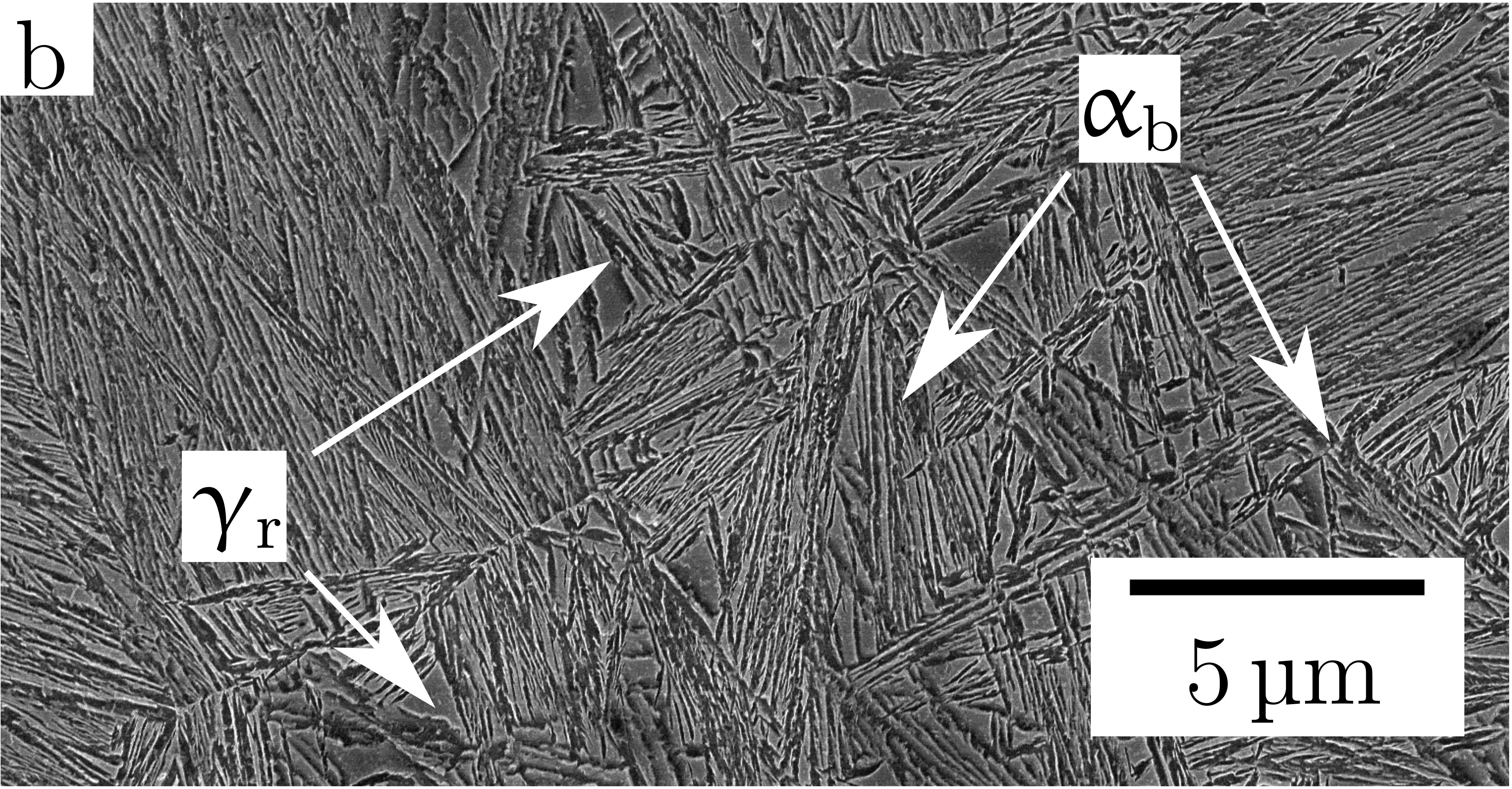
b
α_b
γ_r
5 µm

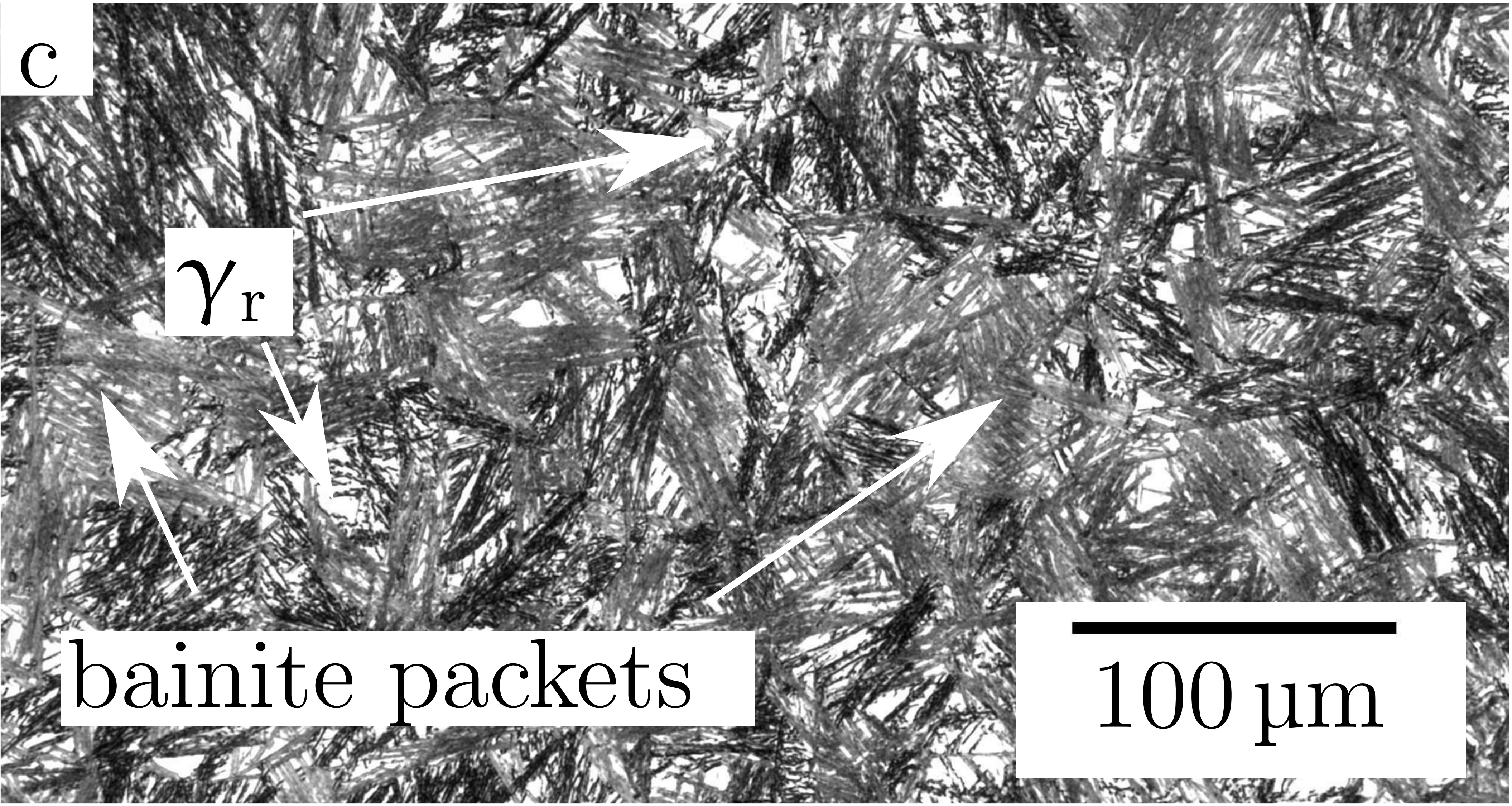
c
γ_r
bainite packets
100 µm

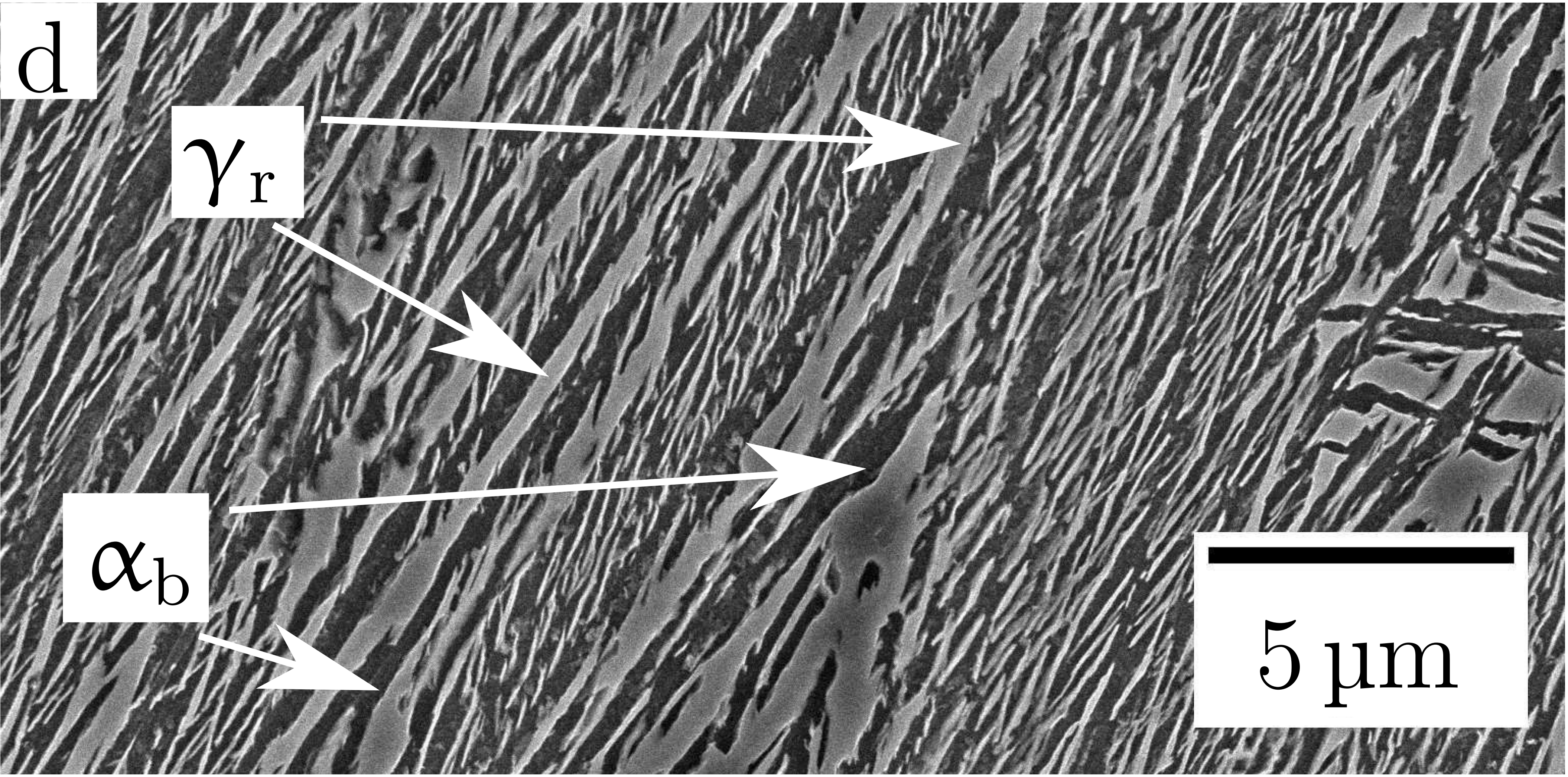
d
γ_r
α_b
5 µm

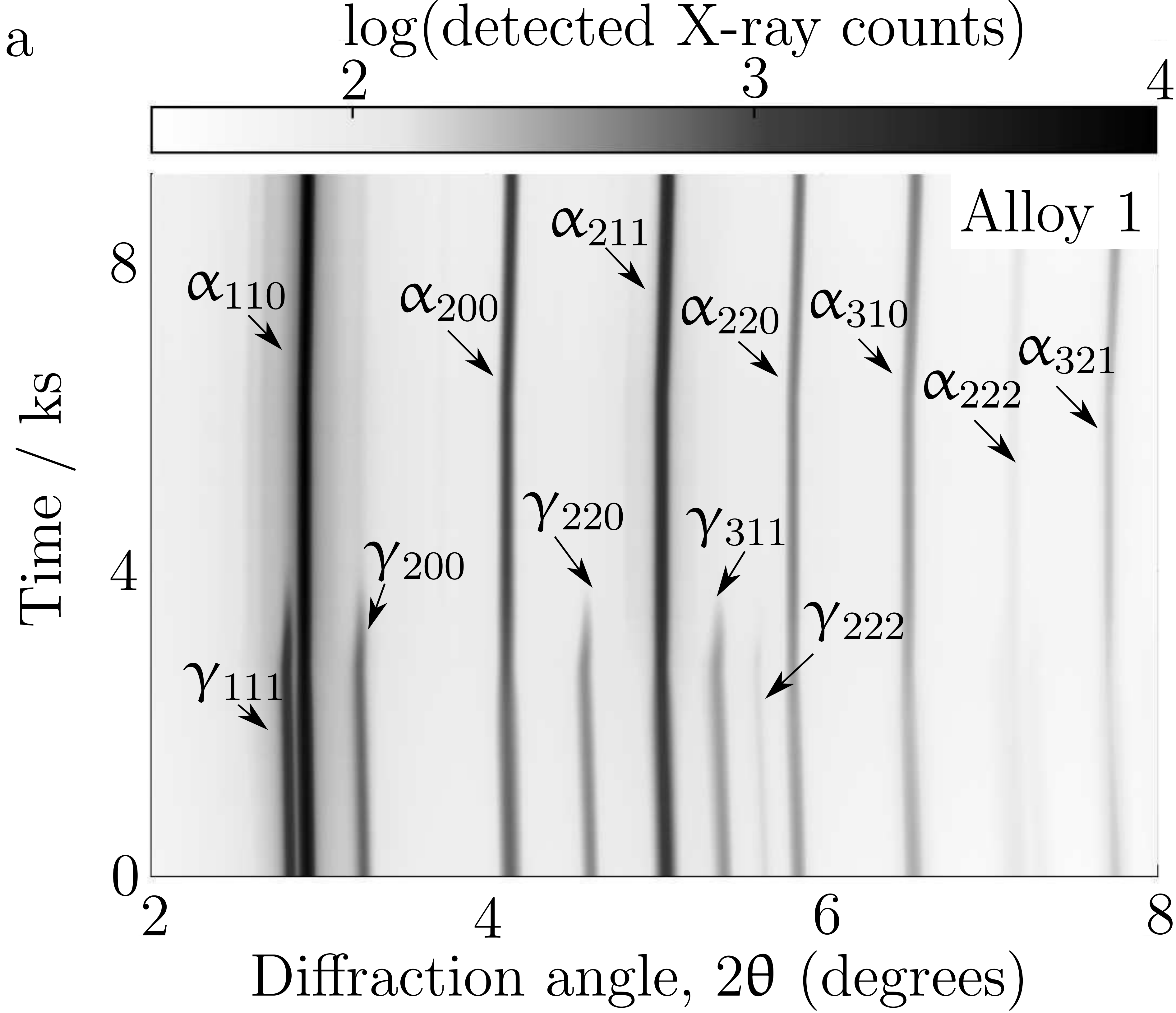
a
log(detected X-ray counts)
2
3
4
Alloy 1
α110
α200
α211
α220
α310
α222
α321
γ220
γ311
γ200
γ222
γ111
Time / ks
8
4
0
2
4
6
8
Diffraction angle, 2θ (degrees)

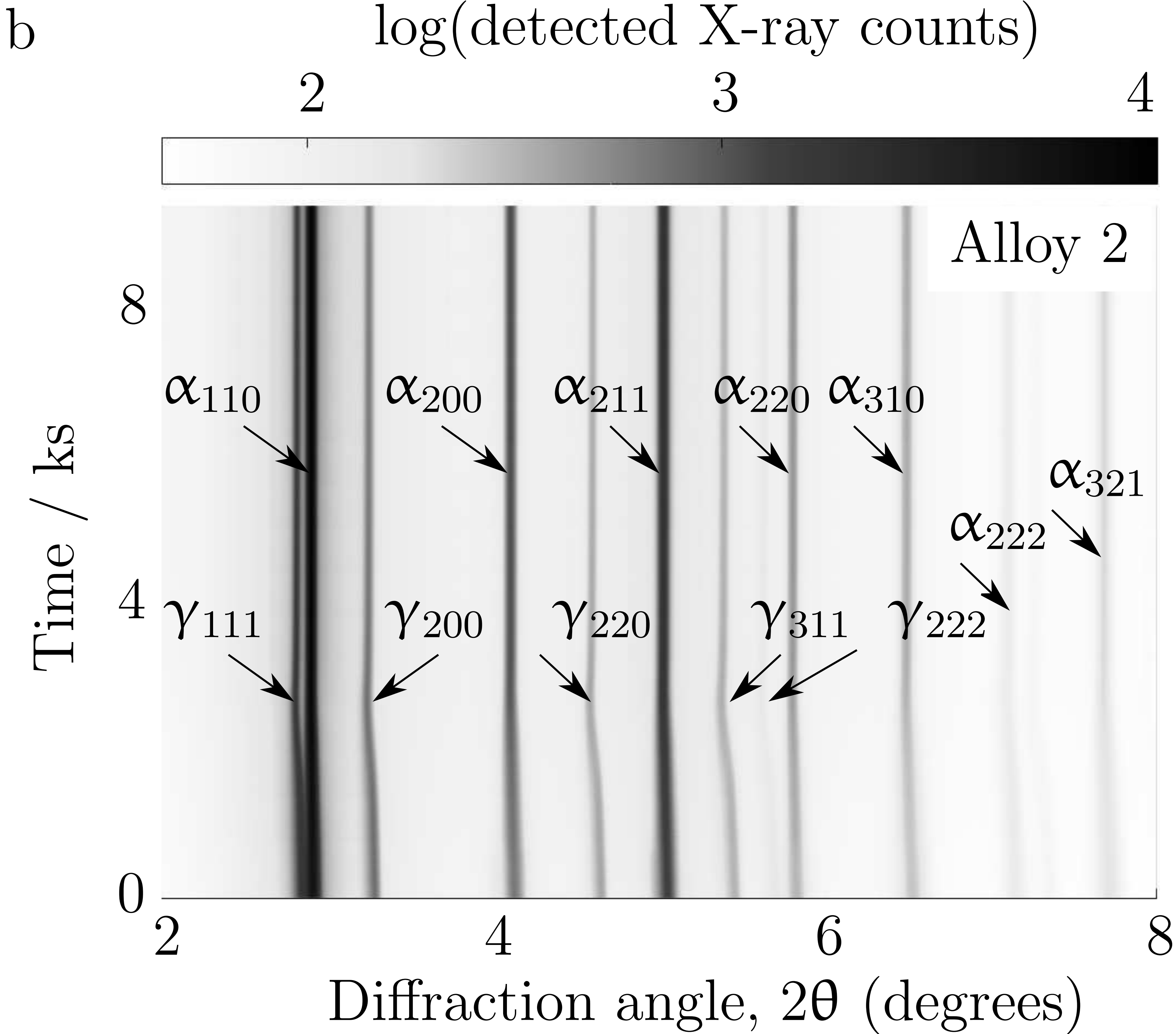
b
log(detected X-ray counts)
2
3
4
Alloy 2
α_{110}
α_{200}
α_{211}
α_{220}
α_{310}
α_{321}
α_{222}
γ_{111}
γ_{200}
γ_{220}
γ_{311}
γ_{222}
Time / ks
8
4
0
2
4
6
8
Diffraction angle, 2θ (degrees)

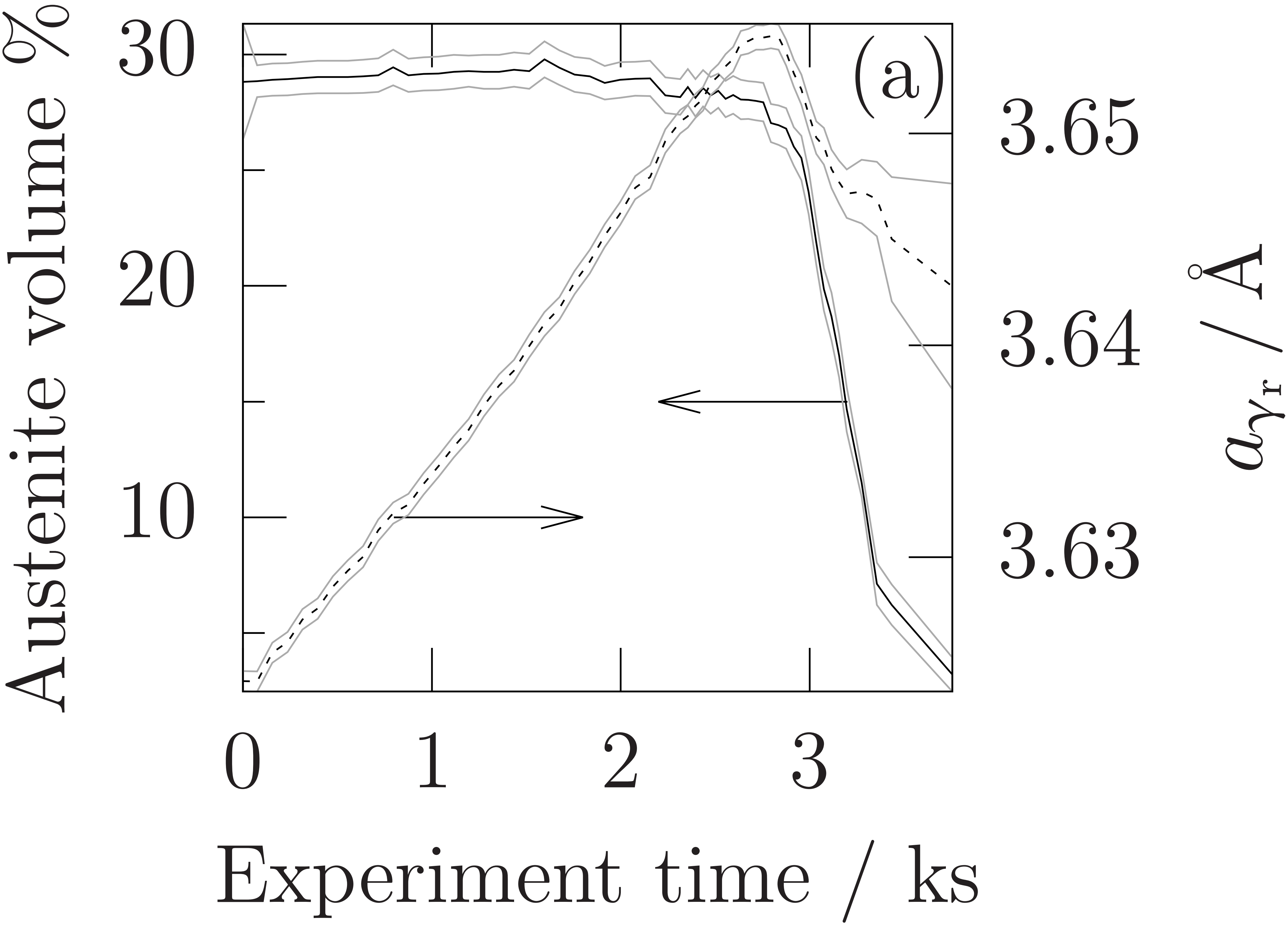

(a)
Austenite volume %
30
20
10
a_{γ_r} / Å
3.65
3.64
3.63
0
1
2
3
Experiment time / ks

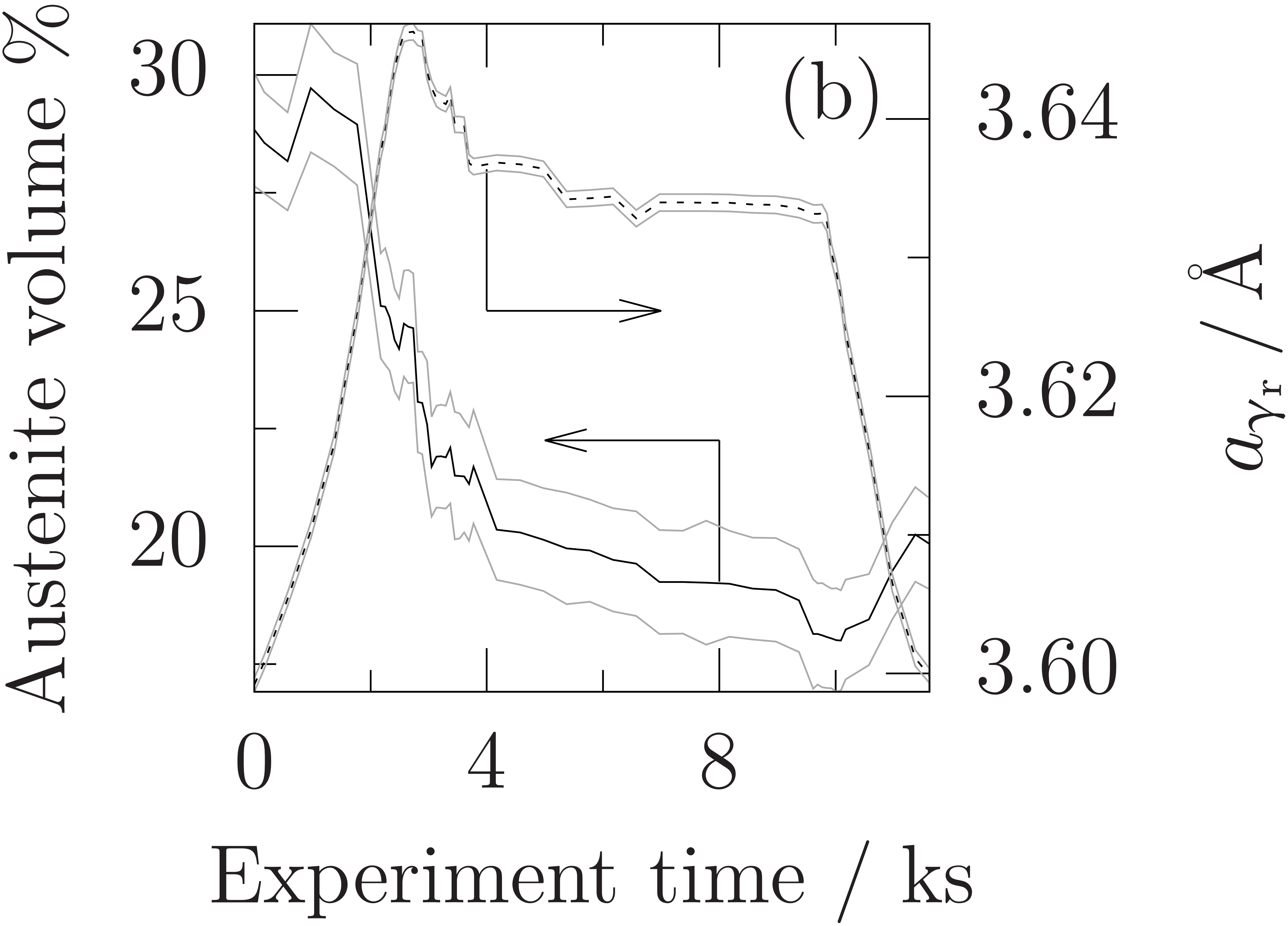
(b)
Austenite volume %
30
25
20
3.64
3.62
3.60
a_{γ_r} / Å
0
4
8
Experiment time / ks

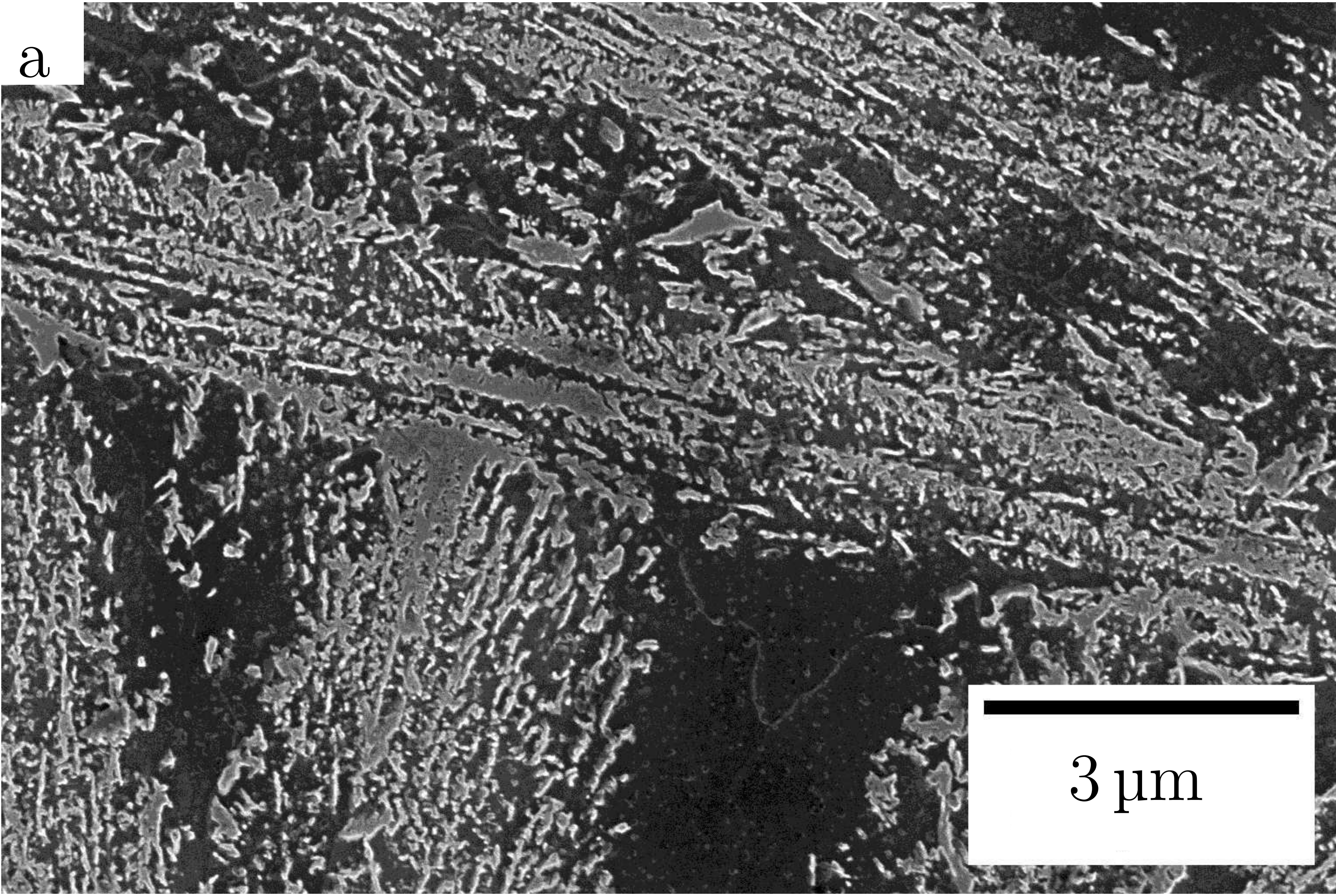
a
3 µm

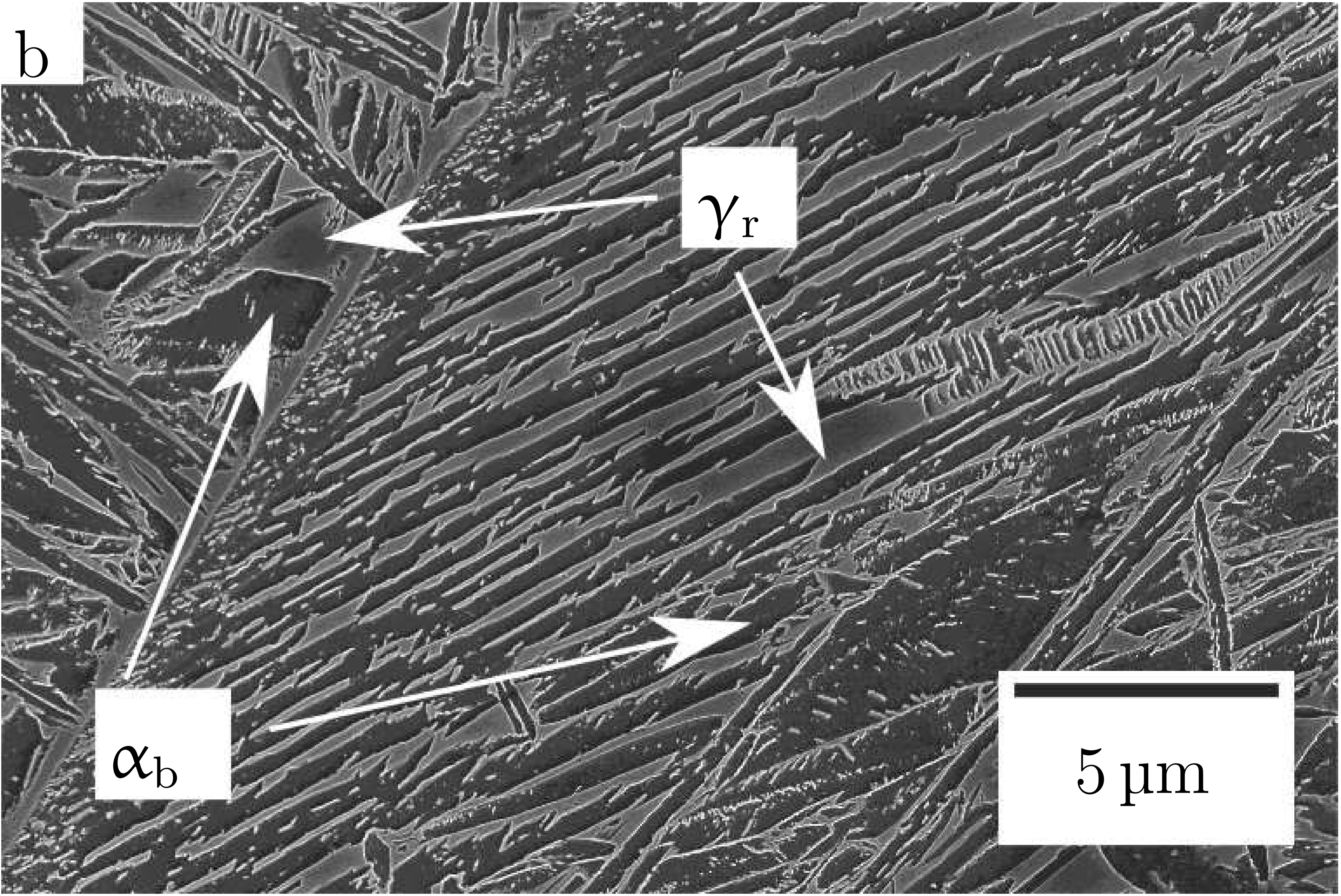
b
γ_r
α_b
5 µm

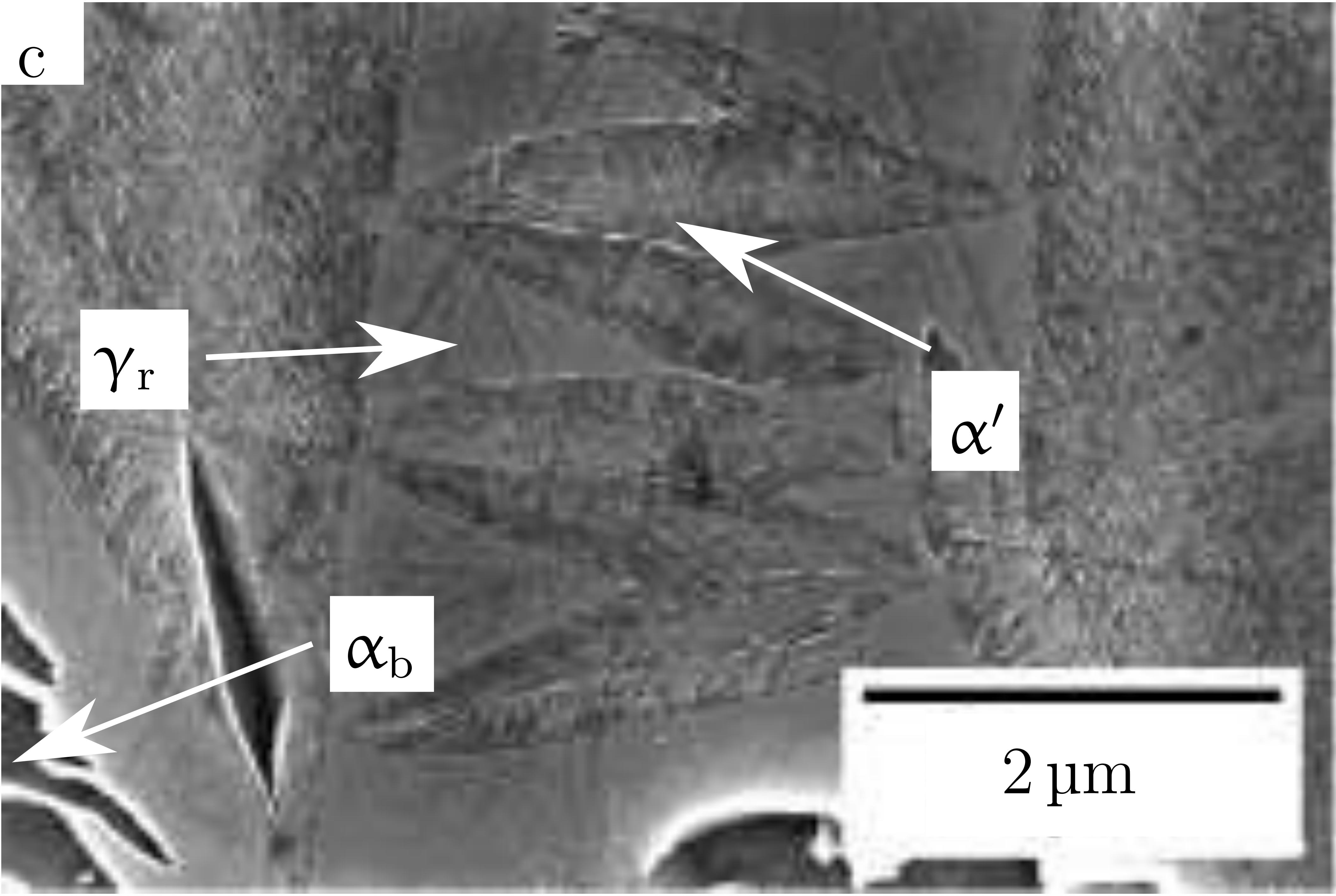
c
γ_r
α'
α_b
2 µm

	C	Mn	Al	Ni	Si	Co	Mo
Alloy 1	0.7	0.02	1.4	3.3	4.0	—	0.25
Alloy 2	0.4	0.15	2.5	13.0	—	4.0	0.3

Table 1: Designed compositions of new alloys. All values are in wt% adn the residue is iron.

	C	Mn	Al	Ni	Si	Co	Mo
Alloy 1	0.72	0.02	1.38	3.40	3.88	—	0.20
Alloy 2	0.45	0.15	2.63	13.2	0.03	3.99	0.30

Table 2: Compositions of novel alloys, as measured during cast production. All values are wt% and the residue is iron.

	γ_r	α_b
Alloy 1	70 ± 30	80 ± 50
Alloy 2	100 ± 30	140 ± 50

Table 3: Stereologically-corrected grain widths, measured perpendicular to the long axis of each plate for samples transformed at 250 °C. All values are in nanometres. Errors are the standard deviation of the individual measurements.

	V_{γ_r} (%)	
	As-transformed	Thermally-exposed
Alloy 1	29 ± 3	3.0 ± 0.7
Alloy 2	28.8 ± 1.2	20.0 ± 1.0

Table 4: Retained austenite volume fraction, V_{γ_r} for both alloys measured before and after thermal exposure during synchrotron experiments.

	a_{γ_r} / nm		
	As-transformed	Peak	Thermally-exposed
Alloy 1	3.6251 ± 0.0005	3.6546 ± 0.0006	3.6127 ± 0.0012
Alloy 2	3.5992 ± 0.0005	3.6463 ± 0.0007	3.5998 ± 0.0005

Table 5: Retained austenite lattice parameter, a_{γ_r}, for both alloys measured before and after thermal exposure during synchrotron experiments. The peak lattice parameter, measured at 500 ℃, is also reported.